PHYSICAL REVIEW D

PARTICLES AND FIELDS

THIRD SERIES, VOL. 3, NO. 7 1 APRIL 1971

Backward π^+p Elastic Scattering from 2.18 to 5.25 GeV/c*†

R. A. SIDWELL,‡ R. R. CRITTENDEN, K. F. GALLOWAY, R. M. HEINZ, AND H. A. NEAL§
Indiana University, Bloomington, Indiana 47401
(Received 30 November 1970)

Differential cross sections are presented for pion-proton elastic scattering in the angular range $-0.6 \gtrsim \cos\theta_{c.m.} \gtrsim -0.98$ at 15 incident π^+ momenta from 2.18–5.25 GeV/c. The angular distributions rise steeply near 180° at all momenta. For laboratory momenta $\gtrsim 2.75$ GeV/c they show a minimum at $u \approx -0.17$ (GeV/c)^2 and a broad maximum near $u \approx -0.6$ (GeV/c)^2. When the data are plotted versus s, for fixed u, a strong signal from the $\Delta(2420)$ resonance is observed. The data are compared with a direct-channel resonance model and with a Regge model which considers the exchange of the N_α, N_γ, and Δ_δ Regge trajectories. The qualitative success of both the direct-channel resonance model and the Regge model lends support to the concept of duality.

I. INTRODUCTION

RESULTS from an optical spark-chamber experiment performed at the Argonne National Laboratory Zero Gradient Synchrotron (ZGS) are reported. The purpose of the experiment was to measure angular distributions for pion-proton elastic scattering in the angular range $-0.6 \gtrsim \cos\theta_{c.m.} \gtrsim -0.98$ at 15 π^+ momenta from 2.18–5.25 GeV/c and five π^- momenta from 2.38–3.00 GeV/c. The π^-p data and π^+p data at 5 GeV/c and lower momenta have been published elsewhere.[1,2]

At the time that this experiment was performed, it was suggested that the π^+p backward angular distribution for momenta less than 3 GeV/c could be satisfactorily explained by direct-channel resonances alone.[3,4] At high energies ($p > 5$ GeV/c) the angular distribution, which is characterized by a peak at backward angles and a minimum near $u \approx -0.2$ (GeV/c)^2,[5] was thought to arise from exchange of the Δ_δ and N_α Regge trajectories.[6] A wrong-signature nonsense zero in the N_α amplitude at $u \approx -0.2$ (GeV/c)^2 would then produce the minimum seen in the experimental data.

At intermediate energies, 2–5 GeV/c, it was proposed that the resonance amplitude was interfering with a nucleon exchange term[7] or Regge-trajectory exchange amplitude. In the Regge interference model for π^-p scattering, several resonances were postulated as recurrences of the known Δ_δ, N_α, and N_γ states.[4] Including these postulated resonances as s-channel resonances, the model was quite successful in fitting the $\pi^-p \to p\pi^-$ 180° cross section,[8] and it was shown that the resonance contribution was very small at momenta above 3 GeV/c. The dip seen in the π^-p data at 2.1 GeV/c at 180° was due to interference between the resonance and Regge amplitudes. Several criticisms were made of this Regge interference model, however, on the grounds that double counting resulted from the model.[9] It was further shown by Dikmen[10] that the π^-p 180° cross section could be described using resonances only.

* Work supported in part by the U. S. Atomic Energy Commission under Contract No. AT(11-1)-2009 and the Indiana University Foundation.

† Portions of this paper are from a dissertation submitted to Indiana University by R. A. Sidwell in partial fulfillment of the Ph.D. degree.

‡ Present address: CERN, Geneva 23, Switzerland.

§ Alfred P. Sloan Foundation Fellow.

[1] R. R. Crittenden, K. F. Galloway, R. M. Heinz, H. A. Neal, and R. A. Sidwell, Phys. Rev. D **1**, 3050 (1970).

[2] J. P. Chandler, R. R. Crittenden, K. F. Galloway, R. M. Heinz, H. A. Neal, K. A. Potocki, W. F. Prickett, and R. A. Sidwell, Phys. Rev. Letters **23**, 186 (1969).

[3] A. S. Carroll, J. Fischer, A. Lundby, R. H. Phillips, C. L. Wang, F. Lobkowicz, A. C. Melissinos, Y. Nagashima, and S. Tewksbury, Phys. Rev. Letters **20**, 607 (1968).

[4] V. Barger and D. Cline, Phys. Rev. **155**, 1792 (1967). These authors found reasonable agreement between the resonance model and π^+p data which existed prior to the experiment reported in Ref. 3.

[5] J. Orear, D. P. Owen, F. C. Peterson, A. L. Read, D. G. Ryan, D. H. White, A. Ashmore, C. J. S. Damerell, W. R. Frisken, and R. Rubinstein, Phys. Rev. Letters **21**, 389 (1968).

[6] C. Chiu and J. Stack, Phys. Rev. **153**, 1575 (1967).

[7] R. M. Heinz and M. H. Ross, Phys. Rev. Letters **14**, 1091 (1965).

[8] The data were measured by S. W. Kormanyos, A. D. Krisch, J. R. O'Fallon, K. Ruddick, and L. G. Ratner, Phys. Rev. Letters **16**, 709 (1966).

[9] R. Dolen, D. Horn, and C. Schmid, Phys. Rev. **166**, 1768 (1968); C. B. Chiu and A. V. Stirling, Phys. Letters **26B**, 236 (1968); Nuovo Cimento **56A**, 805 (1968).

[10] F. N. Dikmen, Phys. Rev. Letters **18**, 798 (1967).

It was with the hope of shedding some light on the question of the phenomenological interpretation of πp backward elastic scattering that we undertook the detailed measurements in the experiment described above. Extant backward $\pi^+ p$ data[11] in this interesting momentum region were rather sparse, and at momenta above 3 GeV/c of rather poor statistical accuracy.

The experimental equipment and procedures are described in Sec. II of this work. The determination of the differential cross sections is outlined in Sec. III and corrections to the data are discussed in Sec. IV. In Sec. V we present the results from this experiment. We compare the results with the Regge[12] and direct-channel resonance[13] models in Sec. VI.

II. EXPERIMENT AND PROCEDURES

A. Experimental Layout

This experiment was performed in the secondary beam No. 1 of the ZGS. The unseparated pion beam used in the experiment was produced by a beam of 12.5-GeV/c protons which was focused onto a 4-in.-long copper target.[14] The momentum of this secondary beam was determined by a bending magnet and a lead collimator. After the collimator the beam passed through two bending magnets and a set of quadrupoles which focused the secondary beam on the 12-in. liquid-hydrogen target used in the experiment. The experimental layout is shown in Fig. 1.

In the region of the liquid-hydrogen target the beam spot averaged about $\frac{3}{4}$ in. in diameter. The momentum spread of the beam was 1% full width at half-maximum (FWHM). The uncertainty in the median momentum was less than 1%. This was determined from time-of-flight studies at several momenta for the pions, protons, and deuterons in the positive beam. The times of flight were measured between the momentum slit and counter B2 (see Fig. 1), a distance of 52.2 ft. The measured difference in time of flight between the pions and deuterons corresponded to a momentum which agreed with the value calculated from the bending magnet excitation curves to within 1%.

To distinguish pions from protons in the beam, a Čerenkov counter was placed just downstream of the collimator. The counter's index of refraction was adjusted at each beam momentum, so that the threshold velocity for Čerenkov light was greater than the kaon and proton velocity and much less than the pion velocity. The beam intensity varied from 30 000 particles (15 000 pions) per burst at 2.18 GeV/c to 150 000 particles (40 000 pions) at 5.00 GeV/c.

As shown in Fig. 1, the beam was detected by counters B1 and B2, which were, respectively, 2×2-in. and 1×1-in. counters of $\frac{1}{4}$-in.-thick scintillator. A_H was an anticounter with a 1-in. hole in it for the beam to pass through and was $\frac{1}{4}$ in. thick. About 10% or less of the beam was intercepted by this counter in normal operation. Anticounters A1–A5 were placed at strategic locations above, below, beside, and downstream of the target. These counters covered most of the solid angle not subtended by the detectors, and reduced the trigger rate by an order of magnitude. Counters $\pi 1$–$\pi 6$ detected the scattered pion and counters P1 and P2 detected the recoil proton. All counters except B1, B2, and A_H were made of $\frac{1}{2}$-in.-thick scintillating plastic. A water-filled Čerenkov counter with a sensitive area of 24×28 in. was placed behind the pion counters $\pi 1$ and $\pi 2$. The purpose of this counter was to suppress triggers from forward scattering events with a slow proton in the pion detector. A signal was required from this Čerenkov counter whenever $\pi 1$ or $\pi 2$ detected a particle.

The beam was defined by $C_G\bar{A}_H$B1 B2, i.e., a coincidence between the gas Čerenkov counter (C_G) and beam counters B1 and B2, with no signal from A_H. The counting rate from C_G was large, since discriminator settings were low to detect the small signals from the phototube viewing the Čerenkov light. Thus spurious beam counts were a hazard. These accidental coincidences were estimated by $C_G'\bar{A}_H$B1 B2, where we deliberately mistimed C_G signals by 50 nsec with respect to $\bar{A}_H$B1 B2. About 2% of the beam counts were accidental coincidences. The trigger for firing the spark chambers was $C_G\bar{A}_H$B1 B2 π p $\bar{A}$, where π means any combination of one or more of the pion counters $\pi 1$–$\pi 6$, p means a signal from P1 and/or P2, and $\bar{A}$ means no signal from any of the anticounters A1–A5. If $\pi 1$ and $\pi 2$ had a signal, we also required a signal from the water-filled Čerenkov counter. The signals from six phototubes in the Čerenkov counter were added together in a mixer. The coincidence $C_G\bar{A}_H$B1 B2 π p $\bar{A}$ was recorded twice using independent circuitry. The fast electronics used was manufactured by EGG.[15] Pulses used in coincidence had 8-nsec widths and anticoincidence pulse widths were set at 16 nsec. A pileup gate was used to suppress some of the triggers having multiple beam tracks. The inputs to the gate were $\bar{A}_H$B1 B2 and A_HB1. A signal from either of these inputs was sufficient to turn off the gate for 1 μsec. The effect of this was to shut off the system for 1 μsec after each beam particle which did not produce a trigger.

[11] Ref. 3; also C. T. Coffin, N. Dikmen, L. Ettlinger, D. Meyer, A. Saulys, K. Terwilliger, and D. Williams, Phys. Rev. **159**, 1169 (1967); J. Banaigs, J. Berger, C. Bonnel, J. Duflo, L. Goldzahl, F. Plouin, W. F. Baker, P. J. Carlson, V. Chabaud, and A. Lundby, Nucl. Phys. **B8**, 31 (1968); W. F. Baker *et al.*, Phys. Letters **23**, 605 (1966); Nucl. Phys. **B9**, 249 (1969); H. Brody, R. Lanza, R. Marshall, J. Niederer, W. Selove, M. Shochet, and R. Van Berg, Phys. Rev. Letters **16**, 828 (1966).

[12] E. Berger and G. Fox, Phys. Rev. **188**, 2120 (1960).

[13] R. R. Crittenden, R. M. Heinz, D. B. Lichtenberg, and E. Predazzi, Phys. Rev. D **1**, 169 (1970).

[14] For $\pi^\pm$ and $K^\pm$ production cross sections, see R. A. Lundy, T. B. Novey, D. D. Yovanovitch, and V. L. Telegdi, Phys. Rev. Letters **14**, 504 (1965).

[15] Edgerton, Germeshausen and Grier, Inc., 35 Congress Street, Salem, Mass. 01971.

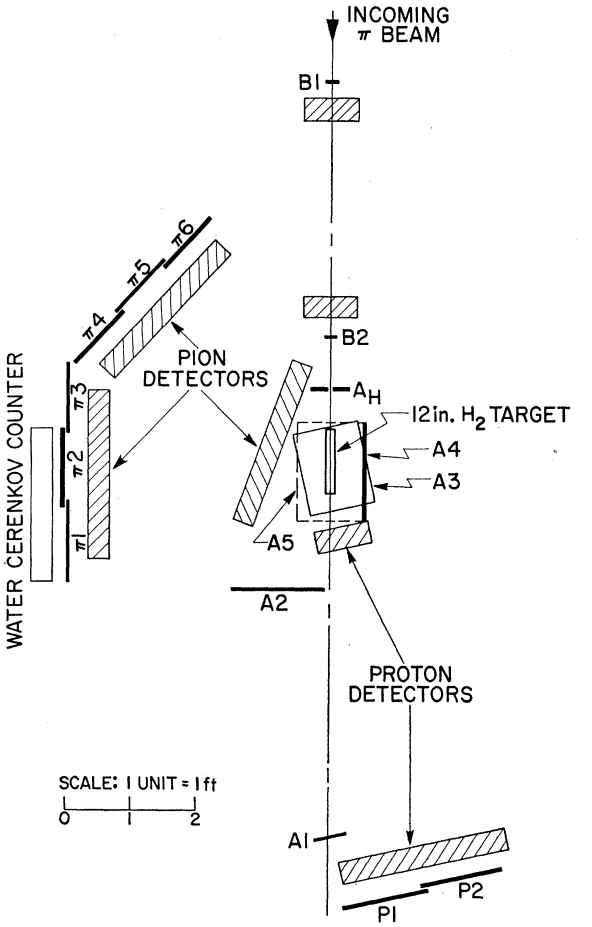

FIG. 1. Experimental layout. The cross-hatched rectangles indicate the optical spark chambers; the solid rectangles are scintillation counters. The pion chambers are referred to as $\rho 1$, $\rho 2$, and $\rho 3$. The proton chambers are labelled Q1 and Q2. $\rho 1$ and Q1 are the two chambers closest to the target.

The incident beam, forward scattered proton, and backward scattered pion trajectories were each measured by two optical spark chambers. The spark chambers are indicated in Fig. 1 by cross hatching. The pion and proton chambers are referred to as ρ and Q, respectively.

The polar angle covered in the lab by the pion chambers was 75°–150°; for the proton chambers 1.5°–24°. These angles correspond to a range of pion angles in the center-of-mass system of $-0.5 \geq \cos\theta_{\text{c.m.}} \geq -0.976$ at 2.18 GeV/c and $-0.7 \geq \cos\theta_{\text{c.m.}} \geq -0.985$ at 5.0 GeV/c.

Each chamber had six $\frac{1}{2}$-in. gaps with 0.001-in.-thick aluminum-foil planes. Neighboring planes were separated by Lucite frames. The chambers were pulsed at 9.5 kV when triggered by the fast electronics. A 150-V clearing field of opposite polarity to the voltage pulse was applied at all times. The chambers were continuously purged with 90% neon, 10% helium gas.

Twenty-one sets of fiducial lights were mounted on the seven spark chambers. A set of fiducial lights consisted of a luminescent panel overlaid with a photographic negative, generating a pattern with an $\times$ and two rectangles.

The chambers were filmed stereoscopically and were viewed from above by mirrors set at 45° with respect to the horizontal. Vertical mirrors were used to reflect the images through a lens into the camera. (The mirrors and the camera location are not shown in Fig. 1.) On each frame of 35-mm film were two views for each of 7 chambers, 21 sets of fiducial lights, and a view of a data box. The data box displayed the date of the run, pion charge, beam momentum, target condition (full or empty), and the roll number and frame number. Pictures of 1145 triggers were taken on each 150-ft roll of 35-mm Kodak Linagraph Shellburst film. In addition, "calibration" pictures were taken at the beginning and end of each roll. In these pictures the chambers were lit from below and from one side in such a way as to illuminate marks etched at 1-in. intervals in two sides of the Lucite frames of the chambers.

The camera was capable of recording one picture per burst. The average number of triggers recorded per burst was 0.6 at 3.00 GeV/c and 0.3 at 5.00 GeV/c.

The operation of the spark chambers was monitored by a closed-circuit television camera so that irregularities in the performance of the chambers or fiducial lights could be readily detected during the running of the experiment.

B. Measurement of Film

We took approximately 250 000 pictures at the 15 incident π^+ momenta. These pictures were scanned by an automatic film reader built at Indiana University named Cathode Ray Ultimate Device, Indiana (CRUDI). CRUDI, based on a Brookhaven National Laboratory design, has been described elsewhere.[16–18] CRUDI was controlled by the CDC 3400 computer at the Indiana University Research Computing Center and was able to scan and measure about 900 35-mm frames an hour. The machine language programming needed to control CRUDI is described in Ref. 18.

The procedure employed in measuring each frame of film was as follows. The film was positioned on the viewing gate using a large fiducial. This fiducial was recognized by its opacity and by its size, 100×400 CRUDI least counts, where one least count is equal to 1.5×10^{-4} in. on the film. Next, the four outermost fiducials on the film were located and their positions measured. On every fiftieth frame all 42 fiducial rectangles were measured. The scan for sparks started in $\rho 1$, the inner pion chamber in Fig. 1. If no sparks were found in $\rho 1$, the

[16] T. Carides, J. G. Cottinham, A. V. Feltman, A. S. Grossman, L. B. Leipuner, J. G. Marinuzzi, and G. C. Schwender, Rev. Sci. Instr. **38**, 1425 (1967).
[17] K. A. Potocki, Ph.D. thesis, Indiana University, 1968 (unpublished).
[18] W. F. Prickett, Ph.D. thesis, Indiana University, 1968 (unpublished).

other chambers were not scanned. For the two outer pion chambers, if more than three sparks were found in the first chamber scanned, the other chamber was not examined.

Scanning for sparks was done down the center of the spark-chamber gap. Sparks were recognized by their opacity (the film is a negative) with respect to the background level, which was measured every 100 frames by a scan in an area free of sparks. Once sparks were found in one gap of the chamber, the locations of the sparks in other gaps were predicted and scanning was done in those restricted areas. This technique avoided the rather time-consuming scan down the full length of the chamber for each gap. If ≤ 3 sparks were found in a view of a chamber, each gap was scanned completely.

The output from CRUDI was written directly onto magnetic tape and consisted of three types of data records: (1) a record at the beginning of each roll of film containing the data-box information; (2) the 42 fiducial positions (repeated every 50 frames); and (3) coordinates, width, and opacity for each spark and measured fiducial. About 400 h of computer time were required to measure the film; this includes time spent eliminating software inadequacies and remeasuring some of the film.

C. Reconstruction of Events

The reconstruction of events proceeded as follows. The first task was to transform the coordinates of the measured fiducials and sparks from the CRUDI coordinate system x_0, y_0 onto a linear coordinate system. The transformation was of the form $x=x_0(a+bx_0^2)$ and $y=y_0(a'+b'y_0^2)$, where the a's and b's were constants determined when CRUDI was calibrated. Next the set of four fiducials measured on every picture was mapped onto the 42 fiducials most recently measured. This determined the over-all magnification, rotation and translation of the coordinate system local to each picture, and the spark coordinates could then be transformed. Finally, the spark and fiducial coordinates were then transformed onto a standard orientation of the coordinate axes. The next step was to filter the sparks. To do this, the two chambers in each arm were treated as a single 12-gap spark chamber filmed in 90° stereo. In each of the two views of the three "12-gap" chambers a least-squares fit to a straight line was made. If a gap contained more than one spark, sparks farthest from the fitted straight line were discarded. (Sparks not discarded are referred to as active sparks.) The active sparks were then filtered by repetitive discarding of the spark farthest from the straight line fitted to the currently active sparks. This filtering stopped when an acceptable χ^2 for the fit was obtained,[19] or only two sparks remained. The sparks in the two views were then paired up and transformed into the three-dimensional laboratory coordinate system. After this procedure, three vectors were formed for the beam, scattered pion, and recoil proton trajectories. A geometrical reconstruction was then made of the vertex of the interaction. This vertex was used as a starting point in a Gauss-Newton iteration which minimized the squares of the perpendicular distances of the sparks from three straight lines which were fitted through them and constrained to intersect at a vertex.

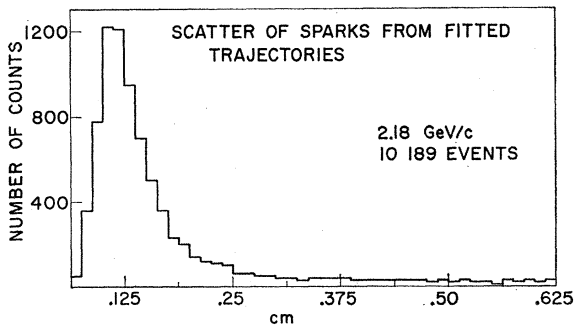

FIG. 2. Histogram of the standard deviation in inches of the scatter of the sparks, in an event, from the fitted vectors.

The "goodness of fit" for each event was calculated by computing σ_{int}, the standard deviation in inches of the scatter of the sparks from the fitted vectors. Figure 2 shows a histogram of σ_{int} for all π^+ data at 2.18 GeV/c. The median scatter was about 1.2 mm in real space.

Depending on momentum, 55–70% of the events could be reconstructed as two-body scatters. Events failed the reconstruction program for a number of reasons. For 8–12% of the data there were no sparks in the inner pion chamber; e.g., the trigger in the π counters may have been caused by a neutral particle. In this case the other chambers were not scanned. For another 5% of the data no single pion track could be formed, usually because there were two or more good tracks in the pion chambers. Fifteen percent of the events failed because no track could be reconstructed from sparks in the proton chambers, either because there were no sparks (~1–2% of all events) or too many (from forward-going inelastic events); 1–4% of the events failed because of multiple beam tracks. If events failed because fiducials were mismeasured, or if the reconstructed data looked in any way suspicious, the film was remeasured. Suspicious rolls were found by noting that the production vertex was displaced, or too many events from the roll had σ_{int} too large, or there were not enough coplanar events compared with other rolls of film at the same momentum. About 10% of the film was remeasured.

Results for each reconstructable event were stored permanently on magnetic tape in a 17-word format containing bookkeeping information, σ_{int}, and the coordinates of the trajectories. Reconstruction was per-

[19] The acceptable χ^2 is $N-2+2[2(N-2)]^{1/2}$, where N is the number of sparks, $N\geq 3$.

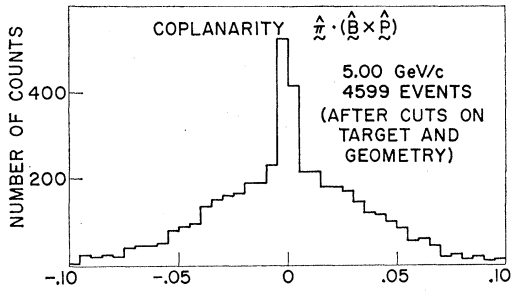

FIG. 3. Distribution of the triple scalar product $C=\hat{\pi}\cdot(\hat{B}\times\hat{P})$ for data at 5 GeV/c.

formed by the CDC 3600 computer of the Indiana University Research Computing Center. About 25 min of computer time was required per roll of film.

D. Fiducial Cuts and Geometrical Efficiency

Cuts on fiducial volume were made under the assumption that all reconstructed events were elastic. This was done by calculating the pion position derived from elastic scattering kinematics from the "proton" angle. Each event was checked to see that, if elastic, it could have been seen by the detectors and the the interaction vertex was in the liquid hydrogen of the target. For the 12-in.-long target we have used events from the center 10.8 in. Cuts were made on the counters and chambers so that detector edges were moved in $\frac{1}{4}$–$\frac{1}{2}$ in. from surveyed positions. No cuts were made where detectors overlapped. Data outside the desired fiducial volume were discarded from the final data sample. The detection efficiency used to weigh the final data was calculated by a Monte Carlo technique at each momentum, and accounted for the geometric acceptance of the apparatus, the absorption of the beam in the target, and the efficiency of the water-filled Čerenkov counter. The detection efficiency was typically 10%.

III. DETERMINATION OF DIFFERENTIAL CROSS SECTIONS

Since the momenta of the final-state particles were not measured, there are two kinematical constraints for an elastic event. The first constraint used was a requirement of coplanarity, defined as the triple scalar product $C=\hat{\pi}\cdot(\hat{B}\times\hat{p})$, where $\hat{\pi}$, $\hat{B}$, and $\hat{p}$ are the unit vectors which describe the trajectories of the scattered pion, beam particle and scattered proton, respectively, in real space. Since elastic scatters are coplanar, they should have a distribution in C centered on zero, with a spread determined by the experimental resolution. Figure 3 shows the distribution of coplanarities for all π^+ data at 5.00 GeV/c. The FWHM of the elastic peak is less than 0.010.

To determine the yield of elastic scatters, data were binned as a function of $\cos\theta_{\text{c.m.}}$, which was calculated from the proton lab angle. The quantity histogrammed for each event was the difference in lab angle between the measured proton angle and the proton angle derived using elastic scattering kinematics and the measured pion angle. This difference is referred to as Δ. Before histogramming Δ, a cut on coplanarity ($|C|\leq 0.0125$) was made in addition to cuts on fiducial volume, production vertex, and the scatter of sparks from the fitted lines ($\sigma_{\text{int}}<0.38$ mm). Δ is plotted in Fig. 4 for π^+ data at 3.75 GeV/c, integrated over all c.m. angles; the FWHM of the elastic peak is ≤ 6 mrad. Note in Fig. 4 that the background is quite flat near the elastic peak, so that background subtraction from under the peak is quite straightforward. Δ was plotted for each c.m. angular bin (e.g., $-0.975\leq\cos\theta_{\text{c.m.}}\leq -0.950$) and background was estimated in each plot by a linear interpolation from bins outside the elastic peak. The background subtraction varied from 0–10% at intermediate angles to 15–40% near 180°, depending on the incident momentum. Reference 2 shows Δ plots at 4.25 GeV/c for $-0.750\leq\cos\theta\leq -0.725$ and $-0.975\leq\cos\theta\leq -0.950$.

The differential cross section was calculated by

$$\frac{d\sigma}{d\Omega}=\frac{Y}{\varphi}\left[\frac{10^{30}}{(A_0)\rho}\times\frac{1}{Z}\times\frac{1}{\Delta\Omega}\right]\mu\text{b/sr},$$

where Y is the yield of elastic events weighted by the reciprocal of the detection efficiency, φ is the net pion flux (for each momentum), A_0 is Avogadro's number, ρ is the density of liquid hydrogen $=0.0706$ g/cm^3, Z is the useable target length (equal to 27.6 cm), and $\Delta\Omega$ is the c.m. solid angle. For most data bins, $\Delta\Omega=d(\cos\theta)d\varphi=(0.025)2\pi$. The total correction to the data from the effects discussed below in Sec. IV was 17% with a normalization error of $\pm 7\%$.

IV. CORRECTIONS TO DATA

A. Efficiency of Counters and Chambers

Each scintillation counter was constructed of a rectangular sheet of scintillating plastic which was viewed through a Lucite light guide by a single 6810A photo tube. The efficiencies of the counters were checked by

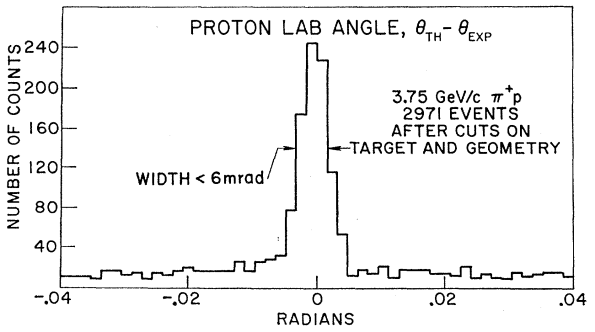

FIG. 4. Distribution of $\theta_{p,\text{lab}}{}^{\text{meas}}-\theta_{p,\text{lab}}{}^{\text{kin}}$ at 3.75 GeV/c for all c.m. angles.

placing them in the beam in coincidence with the beam telescope B1 B2 $\bar{A}_H$. Efficiencies averaged about 99.5% with none less than 99%.

The efficiency of the water-filled Čerenkov counter C_W for detecting relativistic pions ranged from 96–99.5%. The efficiency was mapped on a 2-in. grid over the sensitive area of the counter by placing it in the beam in coincidence with $C_G\bar{A}_H$B1 B2. The efficiency was determined by the ratio $C_GC_W\bar{A}_H$B1 B2/$C_G\bar{A}_H$B1 B2. (The characteristics of the gas-filled Čerenkov counter are discussed in Sec. IV E below.)

The performance of the spark chambers was studied by examining the effects on the data of reconstructing events with information from one chamber omitted. This procedure utilized the redundancy of the detection system. Thus, if the missing chamber was a proton chamber, the beam and pion trajectories were determined as usual and the proton trajectory was defined by the point of intersection of the beam and pion vectors (the production vertex), and the sparks in the remaining proton chamber. The sparks in the remaining chamber were filtered by making a least-squares fit to the straight line determined by the sparks in that chamber and the vertex, which was treated as a spark. Spurious sparks were discarded according to the procedure in Sec. II C.

The purpose of reconstructing events in this manner was to check for angular biases and spark-chamber inefficiencies. If a chamber was inefficient or full of spurious sparks the total number of desired events in a given set of data increased when that chamber was omitted in the reconstruction. An example of this behavior can be seen in Table I, where we list the number of elastic events for each mode of reconstruction in angular bins of width $\Delta\cos\theta_{\text{c.m.}}=0.050$. These data are a sample of bad data from 2.65 GeV/c (π^- beam). Q1 and Q2 are the inner and outer proton chambers, $\rho1$ is the inner pion chamber, $\rho2$ and $\rho3$ are the outer pion chambers. The results obtained by omitting $\rho2$ and $\rho3$ show a net loss of events because the experimental resolution is much poorer when only the inner pion or proton chamber is used in the reconstruction. In the other cases there is an over-all net rise of 2–5%, and in the case where Q2 is omitted we see a 30% rise in the yield at $\cos\theta_{\text{c.m.}}=-0.875$. A scan of this film showed that this behavior was due to a "hot spot" in Q2 centered near $\theta_{p,\text{lab}}\simeq10°$, where the chamber was breaking down. Film in which this type of malfunction was found was discarded. About 20 rolls of film were not used for this reason. The analysis shown in Table I was performed for all of the π^- film and about 15% of the π^+ film. The remaining film was scanned by hand. For the useable film we estimate the combined inefficiency of the spark chambers to be (2±2)%.

TABLE I. Results of chamber efficiency checks. Listed are the number of elastic events found in c.m. angular bins of width $\Delta\cos\theta=0.050$. The data were obtained by omitting the indicated chamber. Q1 and Q2 are the inner and outer proton chambers and $\rho1$ i is the inner pion chamber. $\rho2$ and $\rho3$ are the outer pion chamberss

Bin center $-\cos\theta_{\text{c.m.}}$	Chamber omitted				
	None	Q1	Q2	$\rho1$	$\rho2$ or $\rho3$
0.525	4	4	5	4	3
0.575	4	5	4	6	4
0.625	5	7	4	4	5
0.675	12	11	14	11	10
0.725	23	24	22	26	25
0.775	29	32	37	31	25
0.825	38	39	38	40	36
0.875	65	65	86	66	57
0.925	111	115	115	111	110
0.965	61	64	55	59	61
Totals	352	366	380	358	336

B. Attenuation of Beam in Target

The beam flux recorded by $C_G\bar{A}_H$B1 B2 is the flux at the upstream end of the target. In general, the intensity of the beam as a function of the distance x traversed in the target is

$$I(x)=I_0e^{-x/\lambda},$$

where λ is the pion mean free path in hydrogen. $\lambda\simeq310$ in. for the momentum range of this experiment. Since $x/\lambda\ll1$, the average intensity is therefore $\approx I_0(1-x/2\lambda)$ $\simeq98\%I_0$ for the 12-in. liquid-hydrogen target. Thus, 2% was subtracted from the measured beam flux to account for the attenuation of the beam in the target.

An additional correction of 0.5% was made for interactions of beam particles in the last beam counter B2.

C. Nuclear Interactions of Final-State Particles

Each spark chamber presented 0.006 in. of Al foil and 0.030 in. of Mylar to incident particles. To correct for nuclear interactions of the final-state particles in the liquid hydrogen, Mylar windows of the target and spark chambers, (2.5±1)% was added to the yield of desired events. Two-thirds of this loss occurred in the liquid hydrogen.

D. Multiple Beam Tracks

A scan of the film showed that 6–10% of the pictures contained more than one beam track. Of the events with multiple beam tracks, (30±15)% failed the reconstruction program or could not pass the cut on σ_{int}. Of the reconstructed events, 50% or more had the wrong beam track. Because of the loose cuts on coplanarity and Δ, however, we estimated that only 10–20% of these events were lost. (The beam divergence was ±15 mrad in the vertical direction and ±7 mrad in the horizontal direction). An over-all correction of (3±2)% was made for loss of events with multiple beam tracks.

E. Lepton Content of Beam

The muon content of the beam was measured directly in this experiment by studying the beam attenuation in

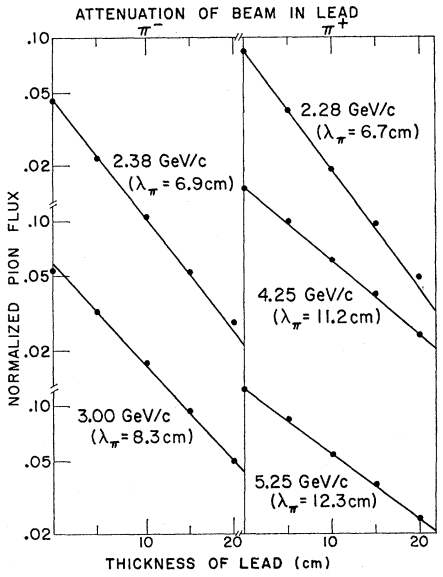

FIG. 5. Normalized beam flux as a function of the thickness of lead in the beam. The measured pion mean free path is indicated at each momentum. Note that the ordinate is logarithmic. The lower part of the ordinate is for the 5.25-π^+ data, the middle part of the ordinate is for the 3.00-π^- and 4.25-π^+ data, and the upper part is for the 2.38-π^- and 2.28-π^+ data. These plots were used to determine the muon contamination in the negative and positive beams.

lead. Lead bricks were placed in the beam between the counters B1 and B2 (see Fig. 1). The pion flux defined by the coincidence $C_G\bar{A}_H$B1 B2 was observed as a function of the thickness of lead. (The pion flux was normalized to a counter telescope BT2, which monitored the flux at the production target.) The results are shown in Fig. 5, where we have plotted the normalized flux as a function of the thickness (t) in cm of the lead in the beam for several π^+ and π^- momenta. The statistical errors are smaller than the symbols used to plot the data. At the low momenta the data lie on a straight line out to t=10–15 cm; at higher momenta a straight line can be drawn through all the data at each momentum.

To determine the muon content of the beam from the results shown in Fig. 5, we used the fact that the muon mean free path in lead, $\sim$190 cm for our beam momenta, is much larger than the values of t used in this study. Since the pions interact strongly, however, their mean free path is much shorter than the muons. The measured pion mean free path λ_π is indicated at each momentum in Fig. 5. For comparison the natural collision length for pions in lead is $L=A/N\sigma_{\text{natural}}=14$ cm, where A is the atomic weight of lead, N is Avogadro's number, and

$$\sigma_{\text{natural}}=\pi(\hbar/m_\pi c)^2A^{2/3}.$$

Using $\lambda_\mu=\infty$ and ignoring electrons, the beam intensity is given by

$$I(t,f)=I_\pi+I_\mu=(1-f)I_0e^{-t/\lambda_\pi}+fI_0,$$

where f is the ratio of muons to particles in the beam, and I_0 is the intensity at t=0. f was assumed to be independent of the beam charge. The results obtained for f were that $f=(1.0\pm0.5)\%$ at 2.28 and 2.38 GeV/c and $(0\pm0.5)\%$ at the higher momenta.

The electron content of the beam, $(6.5\pm1.5)\%$, was estimated from pressure curves from the beam Čerenkov counter. Figure 6 shows a curve for 3.0-GeV/c π^-.

F. Empty-Target Background

Empty-target data were taken at several momenta. The trigger rate as a fraction of the full-target rate varied from 15.5% at 2.38 GeV/c to 28.5% at 4.25 GeV/c. With the target emptied, the yield of good (elastic) events, determined by analyzing the data as though the target were full, was $(0.6\pm0.4)\%$ of the full target yield. About 0.1% of this yield was attributed to interactions with the hydrogen vapor which remained in the target after it was emptied. The remaining events were presumably due to interactions in the side of the target vessel and supports. The correction made to the data for this effect was to subtract $(0.5\pm0.4)\%$ from the yield of good events.

G. Loss of Events from Pion Decay

The minimum laboratory momentum for elastically scattered pions which could be detected by the experimental layout (Fig. 1) was 400 MeV/c at $\theta_{\text{c.m.}}\simeq170°$. Of these 400-MeV/$c$ pions, 4.4% decay between the target and the outer pion chamber. Nearly 100% of these decays are to $\mu\nu$. The maximum opening angle of the muon is 5.6° in the lab for this pion momentum. Thus, for a pion decaying near the target, the measured "pion" angle was deflected by at most 5° in the lab. This maximum deflection, when transformed into the proton lab angle, yields $\Delta\theta_p\approx14$ mrad. Therefore, loss of events due to pion decay was $<1\%$.

V. RESULTS

Differential cross sections from this experiment for backward elastic pion scattering off protons are pre-

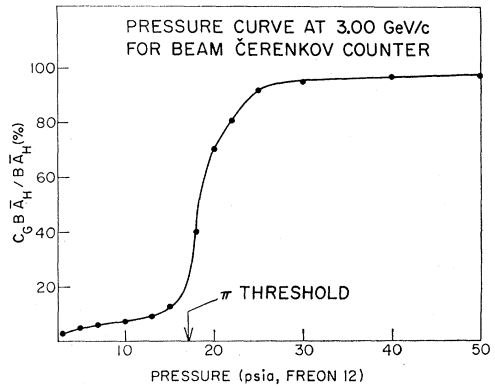

FIG. 6. Ratio C_G B1 B2 $\bar{A}_H$/B1 B2 $\bar{A}_H$ as a function of pressure in the Čerenkov counter for the negative beam. The threshold for producing Čerenkov light in Freon 12 is 17.5 psi (absolute) for 3-GeV/c pions.

TABLE II. Differential cross sections for $\pi^+ p$ backward elastic scattering. Points for which the background subtraction is $\geq 10\%$ are marked with an asterisk (*).

$-\cos\theta_{c.m.}$	u [(GeV/c)^2]	$d\sigma/d\Omega$ (μb/sr)	$d\sigma/du$ [μb/(GeV/c)^2]
2.18 GeV/c			
0.513	−0.668	89.4± 7.5	335 ±28
0.538	−0.626	86.0± 6.4	323 ±24
0.563	−0.584	64.7± 5.5	243 ±21
0.588	−0.542	54.8± 5.0	206 ±19
0.613	−0.500	56.4± 5.1	212 ±19
0.638	−0.459	43.4± 4.4	163 ±17
0.663	−0.417	39.1± 4.2	147 ±16
0.688	−0.375	42.8± 4.4	161 ±17
0.713	−0.333	30.5± 3.7	114 ±14
0.738	−0.291	24.8± 3.3	93 ±12
0.763	−0.249	24.9± 3.3	93 ±12
0.788	−0.208	23.3± 3.2	87 ±12
0.813	−0.166	31.6± 4.5	119 ±17
0.838	−0.124	17.3± 3.4	65 ±13
0.863	−0.082	15.7± 2.5	59 ± 9
0.888	−0.040	22.5± 2.5	84 ± 9
0.913	+0.002	21.9± 2.3	82 ± 9
0.938	+0.044	26.9± 2.7	101 ±10
0.963	+0.086	38.7± 3.2	145 ±12
2.28 GeV/c			
0.513	−0.717	52.8± 5.9	188 ±21
0.538	−0.673	62.8± 5.6	224 ±20
0.563	−0.629	60.7± 5.4	216 ±19
0.588	−0.585	51.9± 5.0	185 ±18
0.613	−0.541	48.1± 4.8	171 ±17
0.638	−0.497	37.6± 4.3	134 ±15
0.663	−0.453	27.7± 3.6	99 ±13
0.688	−0.409	32.9± 4.0	117 ±14
0.713	−0.365	33.1± 4.0	118 ±14
0.738	−0.320	33.3± 4.0	119 ±14
0.763	−0.276	32.9± 4.0	117 ±14
0.788	−0.232	28.3± 3.6	101 ±13
0.813	−0.188	24.2± 3.8	86 ±14
0.838	−0.144	32.5± 4.9	116 ±17
0.863	−0.100	31.8± 3.9	113 ±14
0.888	−0.056	27.3± 2.9	97 ±10
0.913	−0.012	33.0± 3.0	117 ±11
0.938	+0.033	46.0± 3.6	164 ±13
0.963	+0.077	55.1± 3.9	196 ±14
0.978	+0.103	73.8±10.8	263 ±38
2.38 GeV/c			
0.513	−0.767	41.8± 5.8	142 ±20
0.538	−0.721	51.6± 5.4	175 ±18
0.563	−0.674	40.0± 4.5	135 ±15
0.588	−0.628	45.9± 4.8	155 ±16
0.613	−0.581	35.5± 4.2	120 ±14
0.638	−0.535	28.1± 3.8	95 ±13
0.663	−0.489	37.2± 4.3	126 ±15
0.688	−0.442	40.5± 4.5	137 ±15
0.713	−0.396	39.0± 4.4	132 ±15
0.738	−0.349	34.2± 4.1	116 ±14
0.763	−0.303	42.6± 4.6	144 ±16
0.788	−0.257	33.3± 4.0	113 ±14
0.813	−0.210	27.1± 3.9	92 ±13
0.838	−0.164	32.2± 4.6	109 ±16
0.863	−0.117	36.3± 4.4	123 ±15
0.888	−0.071	34.2± 3.4	116 ±12
0.913	−0.025	37.8± 3.2	128 ±11
0.938	+0.022	56.9± 4.1	193 ±14
0.963	+0.068	84.8± 5.0	287 ±17
0.977	+0.095	98.4±13.1	333 ±44
2.75 GeV/c			
0.538	−0.893	30.7± 5.3	88 ±15
0.563	−0.838	31.8± 4.5	91 ±13
0.588	−0.783	38.5± 4.5	110 ±13
2.75 GeV/c			
0.613	−0.728	46.0± 4.8	132 ±14
0.638	−0.673	50.7± 5.1	145 ±15
0.663	−0.619	42.7± 4.7	122 ±13
0.688	−0.564	53.5± 5.2	153 ±15
0.713	−0.509	44.8± 4.8	128 ±14
0.738	−0.454	51.6± 5.2	148 ±15
0.763	−0.399	51.0± 5.1	146 ±15
0.788	−0.344	51.1± 5.1	146 ±15
0.813	−0.289	55.7± 5.3	159 ±15
0.838	−0.235	29.1± 4.2	83 ±12
0.863	−0.180	35.0± 5.0	100 ±14
0.888	−0.125	37.8± 4.1	108 ±12
0.913	−0.070	47.0± 3.5	134 ±10
0.938	−0.015	66.5± 4.4	190 ±13
0.963	+0.040	101.9± 5.5	291 ±16
0.978	+0.073	147.0±12.6	420 ±35
3.00 GeV/c			
0.538	−1.008	17.1± 4.4	44 ±11
0.563	−0.947	24.8± 4.1	64 ±11
0.588	−0.887	30.1± 3.8	78 ±10
0.613	−0.826	26.6± 3.2	69 ± 8
0.638	−0.766	31.7± 3.5	82 ± 9
0.663	−0.705	39.9± 3.9	103 ±10
0.688	−0.644	38.3± 3.8	99 ±10
0.713	−0.584	29.1± 3.3	75 ± 9
0.738	−0.523	36.6± 3.7	95 ±10
0.763	−0.462	28.2± 3.3	73 ± 9
0.788	−0.402	26.1± 3.2	68 ± 8
0.813	−0.341	32.4± 3.3	84 ± 9
0.838	−0.281	20.6± 2.9	53 ± 8
0.863	−0.220	19.3± 3.2	50 ± 8
0.888	−0.159	14.3± 2.4	37 ± 6
0.913	−0.099	18.3± 2.1	47 ± 5
0.938	−0.038	44.9± 3.1	116 ± 8
0.963*	+0.023	59.9± 4.0	155 ±10
0.979	+0.063	67.7± 6.5	175 ±17
3.25 GeV/c			
0.588	−0.989	19.0± 3.4	45.0± 8.0
0.613	−0.923	18.6± 2.8	44.0± 6.6
0.638	−0.857	19.0± 2.6	45.0± 6.2
0.663	−0.790	17.0± 2.5	40.2± 5.8
0.688	−0.724	15.7± 2.3	37.2± 5.6
0.713	−0.658	20.5± 2.7	48.5± 6.4
0.738	−0.591	19.9± 2.7	47.1± 6.3
0.763	−0.525	17.7± 2.5	41.9± 5.9
0.788	−0.458	17.9± 2.5	42.4± 5.9
0.813	−0.392	13.3± 2.0	31.5± 4.8
0.838	−0.326	7.6± 1.6	18.0± 3.8
0.863	−0.259	9.9± 2.2	23.4± 5.1
0.888*	−0.193	5.6± 1.7	13.3± 4.0
0.913*	−0.127	5.4± 1.4	12.8± 3.3
0.938	−0.060	17.1± 2.1	40.5± 5.0
0.963	+0.006	29.1± 2.8	68.9± 6.6
0.979*	+0.048	40.2± 5.8	95.2±13.7
3.50 GeV/c			
0.613	−1.019	13.8± 3.3	30.1± 7.2
0.638	−0.947	14.4± 2.8	31.5± 6.1
0.663	−0.875	11.8± 2.2	25.7± 4.8
0.688	−0.803	14.3± 2.2	31.2± 4.8
0.713	−0.731	11.6± 1.8	25.3± 3.9
0.738	−0.658	10.3± 1.6	22.5± 3.5
0.763	−0.586	11.7± 1.7	25.5± 3.7
0.788	−0.514	15.2± 1.8	33.1± 3.9
0.813	−0.442	9.6± 1.4	21.2± 3.1
0.838	−0.370	8.3± 1.3	18.1± 2.8

TABLE II.—*continued*

$-\cos\theta_{c.m.}$	u [(GeV/c)^2]	$d\sigma/d\Omega$ (μb/sr)	$d\sigma/du$ [μb/(GeV/c)^2]
3.50 GeV/c			
0.863*	−0.298	4.2± 1.3	9.2± 2.8
0.888*	−0.226	5.9± 1.5	12.9± 3.3
0.913*	−0.153	4.1± 1.2	8.9± 2.6
0.938*	−0.081	8.0± 1.3	17.4± 2.8
0.963*	−0.009	16.8± 2.0	36.6± 4.4
0.980*	+0.040	21.9± 3.6	47.7± 7.8
3.75 GeV/c			
0.638	−1.037	9.0± 2.3	18.1± 4.6
0.663	−0.959	8.8± 2.0	17.7± 4.0
0.688	−0.881	8.5± 1.7	17.1± 3.4
0.713	−0.803	10.6± 1.7	21.4± 3.4
0.738	−0.725	12.2± 1.7	24.6± 3.4
0.763	−0.647	10.9± 1.5	22.0± 3.0
0.788	−0.569	14.7± 1.6	29.6± 3.2
0.813	−0.491	9.5± 1.3	19.2± 2.6
0.838	−0.413	10.3± 1.3	20.8± 2.6
0.863	−0.335	13.1± 1.6	26.4± 3.2
0.888*	−0.257	5.9± 1.6	11.9± 3.2
0.913*	−0.180	4.8± 1.2	9.7± 2.4
0.938*	−0.102	6.7± 1.0	13.5± 2.0
0.963*	−0.024	18.4± 1.8	37.1± 3.6
0.980*	+0.029	27.1± 3.7	54.6± 7.5
4.00 GeV/c			
0.639	−1.120	6.0± 2.2	11.3± 4.2
0.663	−1.042	6.4± 1.8	12.0± 3.3
0.688	−0.959	9.4± 1.9	17.6± 3.5
0.713	−0.875	9.4± 1.6	17.6± 3.0
0.738	−0.791	8.7± 1.4	16.3± 2.6
0.763	−0.707	9.7± 1.4	18.2± 2.6
0.788	−0.624	9.9± 1.3	18.6± 2.4
0.813	−0.540	9.6± 1.3	18.0± 2.4
0.838	−0.456	13.1± 1.5	24.6± 2.7
0.863	−0.372	8.8± 1.2	16.5± 2.3
0.888	−0.289	6.4± 1.3	12.0± 2.4
0.913*	−0.205	7.5± 1.3	14.1± 2.4
0.938*	−0.121	4.4± 1.0	8.3± 1.9
0.963*	−0.038	13.8± 1.8	25.9± 3.3
0.980*	+0.021	22.8± 3.2	42.8± 6.0
4.25 GeV/c			
0.663	−1.126	6.2± 2.0	10.9± 3.5
0.688	−1.036	7.1± 1.7	12.5± 3.0
0.713	−0.946	6.7± 1.4	11.8± 2.5
0.738	−0.857	7.8± 1.3	13.7± 2.3
0.763	−0.767	9.7± 1.3	17.0± 2.3
0.788	−0.678	7.0± 1.0	12.3± 1.8
0.813	−0.588	7.4± 1.1	13.0± 1.9
0.838	−0.499	9.6± 1.2	16.8± 2.1
0.863	−0.409	8.0± 1.1	14.0± 1.9
0.888	−0.320	7.8± 1.3	13.7± 2.3
0.913*	−0.230	4.3± 1.1	7.5± 1.9
0.938*	−0.140	5.5± 1.0	9.6± 1.8
0.963*	−0.051	11.7± 1.4	20.5± 2.5
0.980*	+0.012	15.2± 2.3	26.7± 4.0
4.50 GeV/c			
0.667	−1.192	5.0± 2.0	8.2± 3.3
0.688	−1.113	6.6± 1.8	10.9± 3.0
0.713	−1.017	3.9± 1.2	6.4± 2.0
0.738	−0.922	8.8± 1.5	14.5± 2.5
0.763	−0.827	7.5± 1.2	12.4± 2.0
0.788	−0.731	6.1± 1.0	10.0± 1.7
4.50 Ge/Vc			
0.813	−0.636	7.7± 1.1	12.7± 1.8
0.838	−0.541	6.1± 1.0	10.0± 1.7
0.863	−0.445	8.7± 1.2	14.3± 2.0
0.888	−0.350	8.3± 1.3	13.7± 2.1
0.913*	−0.254	5.6± 1.3	9.2± 2.1
0.938*	−0.159	2.0± 0.9	3.3± 1.5
0.963*	−0.064	8.7± 1.3	14.2± 2.1
0.981*	+0.005	16.3± 2.8	26.8± 4.6
4.75 GeV/c			
0.688	−1.189	3.3± 1.3	5.1± 2.0
0.713	−1.088	5.3± 1.5	8.2± 2.3
0.738	−0.987	4.1± 1.0	6.4± 1.6
0.763	−0.886	4.3± 0.9	6.7± 1.4
0.788	−0.784	7.3± 1.1	11.3± 1.7
0.813*	−0.683	5.4± 1.0	8.4± 1.6
0.838	−0.582	8.3± 1.1	12.9± 1.7
0.863	−0.481	8.2± 1.1	12.7± 1.7
0.888	−0.380	5.9± 1.0	9.2± 1.6
0.913*	−0.279	3.5± 1.1	5.4± 1.7
0.938*	−0.177	4.8± 1.0	7.5± 1.6
0.963*	−0.076	7.5± 1.3	11.6± 2.0
0.980*	+0.002	15.8± 2.9	24.5± 4.5
5.00 GeV/c			
0.713	−1.158	0.9± 0.6	1.3± 0.9
0.738	−1.051	3.4± 0.9	5.0± 1.3
0.763	−0.944	4.0± 0.9	5.9± 1.3
0.788	−0.837	4.9± 0.9	7.2± 1.3
0.813	−0.730	4.4± 0.8	6.5± 1.2
0.838	−0.623	6.0± 0.9	8.8± 1.3
0.863*	−0.516	6.2± 1.0	9.1± 1.5
0.888*	−0.409	6.2± 1.1	9.1± 1.6
0.913*	−0.302	2.9± 1.0	4.3± 1.5
0.938*	−0.195	2.1± 0.9	3.1± 1.3
0.963*	−0.088	5.9± 1.2	8.7± 1.8
0.980*	−0.014	15.3± 3.1	22.5± 4.6
5.12 GeV/c			
0.713	−1.192	1.9± 1.3	2.7± 1.9
0.738	−1.082	3.7± 1.4	5.3± 2.0
0.763	−0.972	3.0± 1.1	4.3± 1.6
0.788	−0.863	4.0± 1.1	5.7± 1.6
0.813	−0.753	6.0± 1.3	8.6± 1.9
0.838	−0.643	5.2± 1.2	7.4± 1.7
0.863	−0.533	4.1± 1.0	5.9± 1.4
0.888	−0.424	6.6± 1.4	9.4± 2.0
0.913	−0.314	3.3± 1.1	4.7± 1.6
0.938*	−0.204	3.2± 1.3	4.6± 1.9
0.963*	−0.094	6.0± 1.7	8.6± 2.4
0.980*	−0.018	7.0± 2.7	10.0± 3.9
5.25 GeV/c			
0.725	−1.172	2.1± 0.6	2.9± 0.9
0.763	−1.003	2.5± 0.8	3.5± 1.1
0.788	−0.890	3.0± 0.8	4.2± 1.1
0.813	−0.777	3.4± 0.7	4.7± 1.0
0.838	−0.664	3.1± 0.8	4.3± 1.1
0.863	−0.552	6.2± 1.0	8.6± 1.6
0.888	−0.439	5.1± 1.1	7.0± 1.5
0.913	−0.326	4.3± 1.0	6.0± 1.4
0.938*	−0.213	3.0± 0.9	4.2± 1.3
0.963*	−0.100	4.8± 1.2	6.7± 1.7
0.980*	−0.022	13.7± 2.6	19.0± 3.6

sented in Table II for 15 incident π^+ momenta. These cross sections are from 14 800 events obtained from 234 000 pictures. Data marked with an asterisk (*) indicate where the background subtraction was $>10\%$ of the net signal. The quoted errors are statistical. Results for $d\sigma/du$ as a function of u from this experiment and other experiments in this momentum range are plotted for $\pi^+p \to p\pi^+$ in Fig. 7. u is the square of

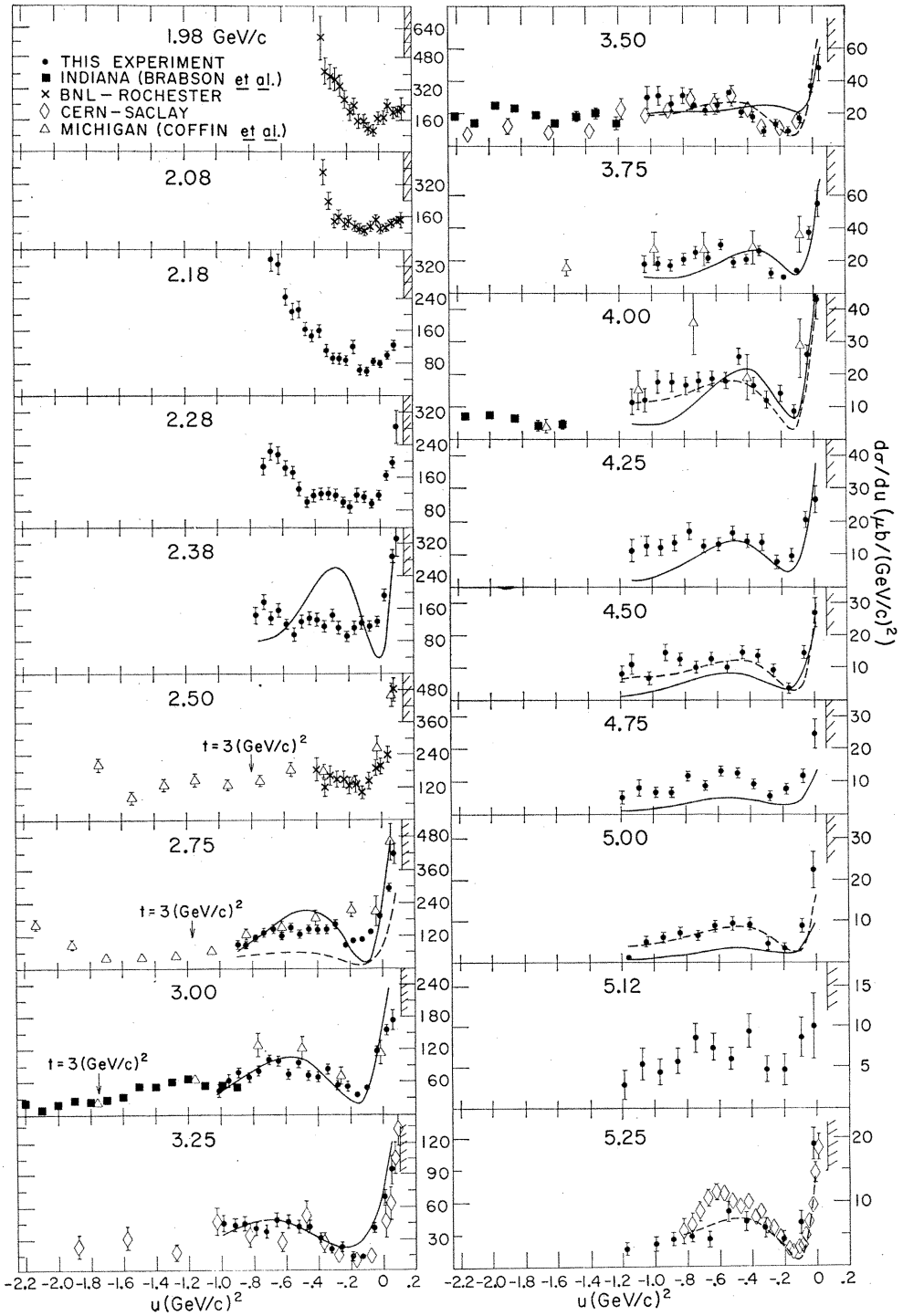

FIG. 7. Angular distributions for backward $\pi^+ p$ elastic scattering. The hatched areas correspond to unphysical values of u. The solid and dashed curves are from resonance model and Regge-model calculations, respectively, which are described in the text. Data from this experiment are represented by the solid circles. Also shown are data from Indiana (Ref. 20), BNL-Rochester (Ref. 3), CERN-Saclay (Ref. 21) and University of Michigan (Ref. 22).

the four-momentum transfer between the incoming pion and outgoing proton. Data from experiments by Indiana,[20] the BNL-Rochester collaboration,[3] the CERN-Saclay collaboration,[21] and the University of Michigan[22] are also shown. Data from this experiment are represented by solid circles.

At momenta ≥ 2.75 GeV/c the π^+p distributions are remarkably similar, being characterized by a steep, narrow backward peak, a dip at $u\approx -0.17$ (GeV/c)^2 and a broad maximum centered around $u\approx -0.6$ (GeV/c)^2. This same structure persists in angular distributions taken at momenta as high as 13 GeV/c.[5] However, the backward peak disappears at 2.08 GeV/c (as shown in Fig. 7). The pronounced dip at $u=-0.17$ also disappears at this momentum. In Fig. 8 we plot $d\sigma/du(u=\text{const})$ vs s, the square of the total c.m. energy $E_{\text{c.m.}}$, for s from 4–12 GeV^2. This shows the behavior of the $\pi^+p\rightarrow p\pi^+$ cross section as we pass through the various resonances in the $I=\frac{3}{2}$ amplitude. The data are from this experiment and Refs. 3 and 5. Note the large bump centered on the $\Delta(2420)$ at $s\simeq 6$ GeV^2. This $\Delta(2420)$ signal is strongest near the backward direction ($u\approx 0$). At $s\simeq 8$ GeV^2 ($E_{\text{c.m.}}\simeq 2.8$ GeV) the cross sections also show a hint of structure.

VI. THEORY

A. Regge Theory

A considerable amount of pion-nucleon scattering data has now been accumulated[23] and a large number of models which attempt to explain these data have been proposed.[13,24,25] In the Regge model for π^+p backward elastic scattering, it is predicted that the angular distributions are dominated by the N_α, and to a lesser extent the N_γ and Δ_δ trajectories.[6,12,24] One way in which to investigate which trajectories are exchanged in backward πp elastic scattering is to determine an effective Regge trajectory from the data. The differential cross section for fermion Regge exchange can be approximated by the model-independent form

$$d\sigma/du=F(u)s^{2(\alpha_{\text{eff}}-1)},$$

where α_{eff} is the effective Regge trajectory. To fit the data with this simple expression, we write

$$\ln(d\sigma/du)=\ln F(u)+(2\alpha_{\text{eff}}-2)\ln s,$$

and then plot $\ln(d\sigma/du)$ at fixed u versus $\ln s$ to determine α_{eff} at various values of u. A logarithmic plot of

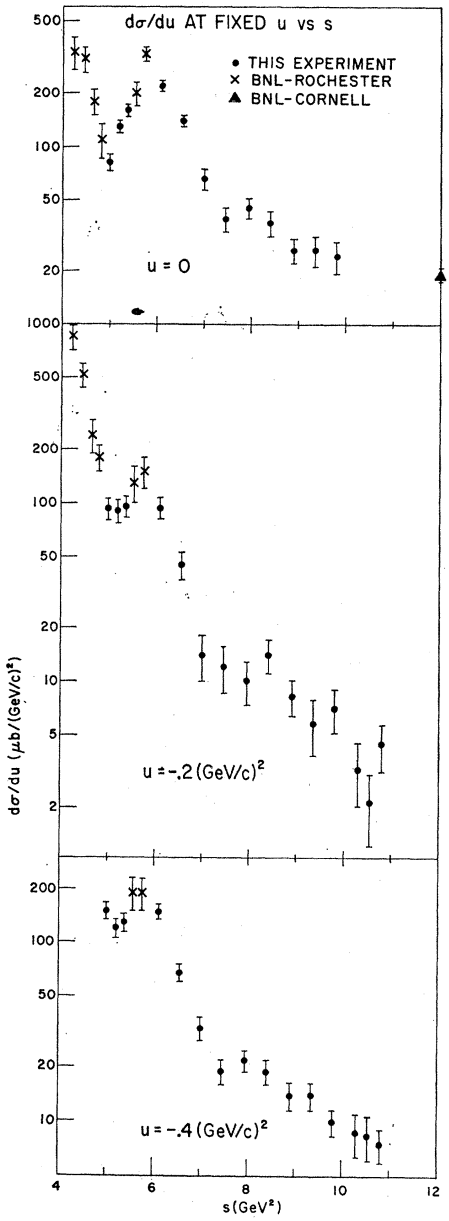

FIG. 8. Differential cross sections at several fixed values of u for s in the range 4–12 GeV^2. Data are from this experiment and Refs. 3 and 5.

$d\sigma/du$ at fixed u vs s is shown in Fig. 9 for $0\geq u\geq -1.0$ (GeV/c)^2. The data are from this experiment and Refs. 5 and 21. A plot of α_{eff} vs u is shown in Fig. 10 where we use only the π^+p data from this experiment for $5.25\geq p_{\text{lab}}\geq 3.25$ GeV/c, corresponding to $10.8\geq s\geq 7.0$ (GeV/c)^2, to calculate α_{eff}. For comparison $\alpha(u)$ is drawn in Fig. 10 for the Δ_δ, N_α, and N_γ trajectories. The effective trajectory, except possibly in the neighborhood of $u\approx -0.2$ (GeV/c)^2, is in good agreement with the N_α trajectory. In Regge models with wrong-signature nonsense zeros, the amplitude for N_α exchange is zero for $\alpha=-\frac{1}{2}$, a value attained for the N_α

[20] B. B. Brabson, R. Crittenden, R. M. Heinz, R. C. Kammerud, H. A. Neal, H. W. Paik, and R. A. Sidwell, Phys. Rev. Letters 25, 553 (1970).
[21] Banaigs *et al.* in Ref. 11.
[22] Coffin *et al.* in Ref. 11.
[23] See, e.g., the compilation by G. Giacomelli, P. Pini, and S. Stagni, CERN/HERA Report No. 69-1, 1969 (unpublished).
[24] For a recent review of Regge-model results, see G. E. Hite, Rev. Mod. Phys. 41, 669 (1969).
[25] For a comparison of the Regge pole and Regge cut models, see E. Berger and G. Fox, ANL/HEP Report No. 7019, 1970 (unpublished).

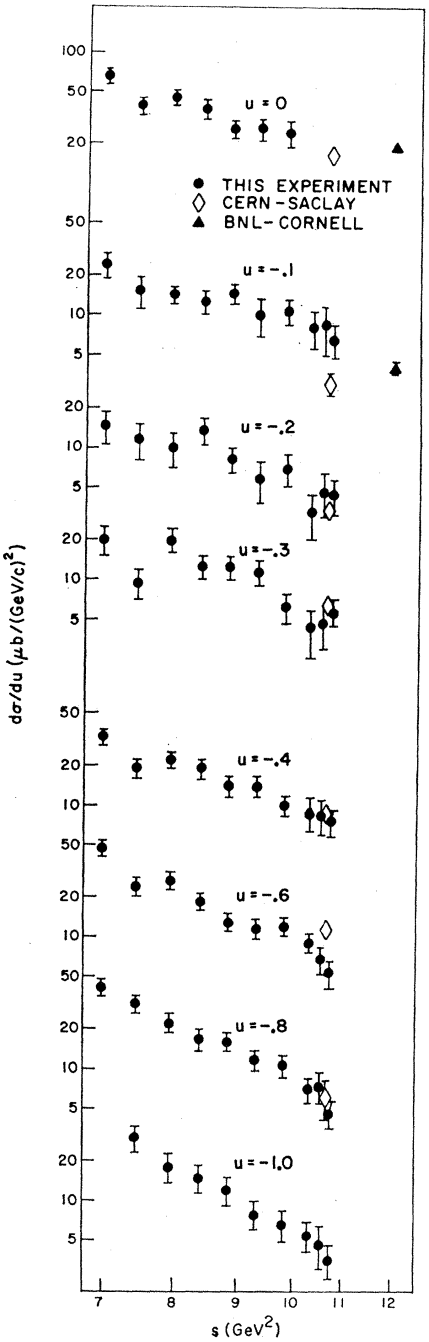

FIG. 9. Logarithmic plot of $d\sigma/du$ at fixed u vs s. These data were used to determine the effective trajectory shown in Fig. 10.

near $u\approx -0.15$ or -0.2 $(\mathrm{GeV}/c)^2$.[12] This zero means that the Δ_δ amplitude should be dominant for u in this region. This is the behavior observed in Fig. 10. The conclusion to be drawn from this analysis is that the effective trajectory for π^+p backward elastic scattering is consistent with the u-channel exchange of the N_α, N_γ, and Δ_δ trajectories at least for $|u|\leq 1.0$ $(\mathrm{GeV}/c)^2$ and $5.25\geq p_{\mathrm{lab}}\geq 3.25$ GeV/c. Over this range of angles and momenta there appears to be no need to include

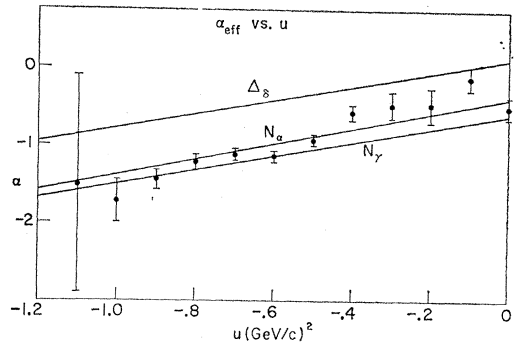

FIG. 10. Effective trajectory for π^+p backward elastic scattering, determined from the data of this experiment in the momentum range $5.25\ \mathrm{GeV}/c\geq p\geq 3.25\ \mathrm{GeV}/c$, which corresponds to $10.8\ (\mathrm{GeV}/c)^2\geq s\geq 7.0\ (\mathrm{GeV}/c)^2$. The Δ_δ, N_α, and N_γ trajectories are shown for comparison.

Regge cuts[26] in the amplitude. These would lead to a less steep effective trajectory. For a plot of α_{eff} vs t for forward and intermediate angles for both π^+p and π^-p scattering, see Refs. 20 and 27.

We have calculated the angular distributions and polarization for π^+p backward elastic scattering using Δ_δ and N_α exchange.[28] The parametrization employed was that of Berger and Fox.[12] Results from this calculation are shown by the dashed curves in Fig. 7. The agreement with the cross-section data is quite good for $p>3.0$ GeV/c. The model also agrees well with the backward π^+p polarization data below 3.0 GeV/c.[29] The minimum in the differential cross sections at $u\simeq -0.15$ $(\mathrm{GeV}/c)^2$ was obtained in this model by the nonsense zero in the N_α amplitude at $\alpha=-\frac{1}{2}$.

B. Direct-Channel Responses

It has been proposed[13] that the πp backward angular distributions, for moderate values of s, arise from a sum of direct-channel resonances. The direct-channel resonance model (DCRM) assumes that all resonances in the πp system lie on Regge trajectories of uniform slope. In order to fit the data with the DCRM it is necessary to postulate a large number of resonances as Regge recurrences of known resonances. The widths and elasticities of the recurrences are generated from

$$\Gamma=\Gamma_1+a(M-M_1)$$

and

$$X=X_1\exp[-b(M^2-M_1{}^2)],$$

where Γ_1, X_1, and M_1 are the width, elasticity, and mass of the lowest-lying state on the trajectory and Γ

[26] F. Henyey, G. L. Kane, J. Pumplin, and M. H. Ross, Phys. Rev. **182**, 1579 (1969); R. L. Kelly, G. L. Kane, and F. Henyey, Phys. Rev. Letters **24**, 1511 (1970).

[27] G. Hohler, J. Baacke, H. Schaile, and P. Sondegger, Phys. Letters **20**, 79 (1966). See also the recent compilation of G. Fox and C. Quigg, LRL Report No. UCRL 20001, 1970 (unpublished).

[28] The Regge calculations were done by P. Tomlinson, Indiana University.

[29] D. Sherden, N. Booth, G. Conforto, R. Esterling, J. Parry, J. Scheid, and A. Yokosawa, Phys. Rev. Letters **25**, 898 (1970).

and X are the width and elasticity of a recurrence of mass M. a and b are adjustable parameters. For the Δ_δ trajectory $a=0.16$ and $b=0.54$ $(\mathrm{GeV}/c)^{-2}$ describe the widths and elasticities of the recurrences fairly well.

Crittenden *et al.*[13] used the DCRM to fit backward different cross sections for $\pi^+p\to p\pi^+$ in the angular range $120°\leq\theta_{\mathrm{c.m.}}\leq 180°$ for lab momenta from 2.18 to 5.0 GeV/c. Five trajectories, which had as lowest-mass states the $\Delta(1236)\ \frac{3}{2}^+$, $\Delta(1630)\ \frac{1}{2}^-$, $\Delta(1670)\ \frac{3}{2}^-$, $\Delta(1690)\ \frac{3}{2}^+$, and $\Delta(1930)\ \frac{1}{2}^+$ resonances, were employed, with a total of eight parameters required to obtain the widths and elasticities of the recurrences of these states. The agreement of the model with the data is quite good, especially for momenta above 2.28 GeV/c; the DCRM was quite successful at obtaining the dip in cross section at $u\simeq -0.2$ $(\mathrm{GeV}/c)^2$ seen at momenta above 2.38 GeV/c.

It should be pointed out that, in spite of the success of the cross-section fits, the amplitudes obtained in Ref. 13 do not give a very good account of the polarization at backward angles.[29] In addition, the widths obtained for some of the Δ_α recurrences are larger than the masses of the resonances.

More recently we have made fits to the π^+p data using a version of the DCRM which requires only one free parameter. We add the angular distributions from resonances on five trajectories as before, but for the $\Delta(1690)\ \frac{3}{2}^+$ we substitute a trajectory based on the $\Delta(1890)\ \frac{5}{2}^+$. [The $\Delta(1890)\ \frac{5}{2}^+$ is considered by the Particle Data Group[30] to be more likely to exist than the $\Delta(1690)\ \frac{3}{2}^+$.] The elasticities of the recurrences are now assumed to drop more rapidly with s,

$$X=X_1\exp[-\beta(M^2-M_1^2)^2-\gamma(M^2-M_1^2)],$$

where the parameters β and γ were fixed by fitting the elasticities of the Δ_δ recurrences. Assuming 10% uncertainties in the elasticities of the $\Delta(1950)$, $\Delta(2420)$, $\Delta(2850)$, and $\Delta(3230)$, the fitted values of β and γ are $\beta=40$ $(\mathrm{GeV}/c)^{-4}$ and $\gamma=2.7$ $(\mathrm{GeV}/c)^{-2}$, with $\chi^2=5$. These same constants are used to predict the elasticities of the other four trajectories used in the model. The widths of the resonances are generated by $\Gamma=\Gamma_1+a(M-M_1)$, where a is assumed to be the same constant ($a=0.16$) for all the trajectories and is determined from a fit to the width of the Δ_δ recurrences. The resonance amplitude employed has a nonrelativistic Breit-Wigner distribution with exponentially damped tails

$$A=\frac{\frac{1}{2}\Gamma[(E-M)+i\frac{1}{2}\Gamma]}{(E-M)^2+\frac{1}{4}\Gamma^2}\exp\left[-4d\left(\frac{E-M}{\Gamma}\right)^2\right],$$

where d is a free parameter in the model—the only free parameter is this version of the DCRM. We have used this model to fit 66 π^+ polarization data from 2.50 to 3.75 GeV/c from Ref. 29 and 174 $\pi^+p\to p\pi^+$ data from this experiment at lab momenta from 2.38 to 5.00 GeV/c. The χ^2 for the fit to these 240 data was 2725; the χ^2 for the polarization data alone was 554. The results obtained for this solution, indicated by the solid curves in Fig. 7, are reasonably good. At all momenta this simple model predicts the backward peaking of the angular distributions and the minimum at $u\approx -0.2$ $(\mathrm{GeV}/c)^2$. The model agrees qualitatively with the polarization data at momenta up to 3.25 GeV/c, and for cross-section data between 2.75 and 4.5 GeV/c.[31] The predicted differential cross section is low at 5.0 GeV/c and exhibits excessive oscillations at 2.75 GeV/c and below. The damping factor obtained for this fit is $d=0.038$, so that at energies one full width Γ away from the resonance energy the damping amounts to 14%.

C. Duality

We have seen that the π^+p backward elastic scattering data at intermediate energies can be described either by exchange of Reggeized baryon trajectories or by summing the amplitudes of direct-channel resonances. From a study of finite-energy sum rules (FESR), Dolen, Horn, and Schmid[9] have suggested that the Regge amplitude (for backward scattering) is given by the smoothed-out resonance contribution. This consequence of the FESR is usually called "weak" duality. The consistency between the results of the DCRM and the Regge model of Berger and Fox,[12] along with the relatively good agreement of both models with the data, lends support to the concept of duality. A detailed comparison of the amplitudes from these two models is given in Ref. 31.

ACKNOWLEDGMENTS

We are indebted to the Argonne ZGS staff for their support throughout the experiment. We appreciate the contributions of Dr. J. P. Chandler, Dr. H. J. Martin, Dr. D. Meyer, Dr. K. Potocki, and Dr. W. Prickett to the initial stages of the experiment, and of P. Tomlinson to the theoretical calculations. Dr. D. B. Lichtenberg, Dr. E. Predazzi, and Dr. Marc Ross made substantial contributions to our theoretical understanding of the data.

[30] Particle Data Group, Rev. Mod. Phys. **41**, 109 (1969); **42**, 87 (1970).

[31] The comparison of the resonance model with the polarization data and more details on the model are given in P. G. Tomlinson, R. A. Sidwell, D. B. Lichtenberg, R. M. Heinz, R. R. Crittenden, and E. Predazzi, Nucl. Phys. B25, 443 (1971).